 doi:10.20944/preprints202210.0236.v1

Article

Pyroelectric and piezoelectric voltage coefficients of blue luminescent organic lead-free perovskite MDABCO-NH_4I_3 electrospun nanofibers

Rosa Baptista [1], Gonçalo Moreira [1], Bruna Silva [1], João Oliveira [1], Bernardo Almeida [1], Cidália Castro [2], Pedro V. Rodrigues [2], Ana Machado [2], Michael Belsley [1*] and Etelvina de Matos Gomes [1]

[1] Centre of Physics of Minho and Porto Universities (CF-UM-UP), University of Minho, Campus de Gualtar, 4710-057 Braga, Portugal
[2] Institute for Polymers and Composites, University of Minho, Campus de Azurém, 4800-058 Guimarães
* Corresponding author: belsley@fisica.uminho.pt

Abstract: Lead-free ferroelectric perovskite N-methyl-N'-diazabicyclo[2.2.2]octonium)–ammonium triiodide, MDABCO-NH_4I_3, nanocrystals are embedded in three different polymer fibers fabricated by the electrospinning technique. The nanofibers, which are very flexible and have a high Young modulus, behave as active piezoelectric energy harvesting sources that produce a piezoelectric voltage coefficient up to g_{eff} = 3.6 VmN^{-1} and show a blue intense luminescence band at 325 nm. In this work, the pyroelectric coefficient is reported for the MDABCO-NH_4I_3 perovskite inserted in electrospun fibers. At the ferroelectric-paraelectric phase transition, the embedded nanocrystals display a pyroelectric coefficient as high as 194×10^{-6} $Cm^{-2}k^{-1}$, within the same order of magnitude as that reported for the state-of-the-art bulk ferroelectric triglycine sulfate (TGS). The perovskite nanocrystals embedded into the polymer fibers remain stable, and no degradation is caused by oxidation.

Keywords: organic lead-free perovskites; piezoelectric crystals; nanofiber composites; electrospinning; blue luminescence; functional organic materials

1. Introduction

Ferroelectrics are inherently piezoelectric and pyroelectric materials; that is, they are able to produce an intrinsic electrical potential difference in response to an applied force (or originate a mechanical movement due to an applied electric field) and a temperature gradient, respectively.

Valasek discovered the first ferroelectric, Rochelle salt or potassium sodium tartrate tetrahydrate [KNaC4H4O6] (4H2O), in 1920 and was in fact the first semiorganic molecular ferroelectric crystal that is also non-toxic [1-2].

Among ferroelectrics, inorganic perovskites, formula ABX_3 (A, B = metal cations, X = anion; usually an oxide), are a well-known family of solid-state inorganic compounds finding applications like capacitors, sensors, actuators, etc. The best known are metal oxides such as strontium, barium, or lead titanate ($SrTiO_3$, $BaTiO_3$, PbTiO3, respectively), their solid solutions such as Pb(Zr,Ti)O_3 (PZT), niobates such as PZN ($PbZn_{1/3}Nb_{2/3}O_3$) (PZN), ($PbMg_{1/3}Nb_{2/3}O_3$) (PMN) and lithium niobate LiNbO3). These materials have, until now, been used largely by several industries due to their functional properties, combining ferroelectricity with nonlinear optical and electro-optic effects as well as multiferroicity [3-4].

So far, the commercially available piezoelectrics are dominated by inorganic perovskites, namely PZT-based materials, and polymers such as polyvinylidene difluoride (PVDF) and its modifications such as PVDF-TrF. They have been applied in actuators, sensors, transducers, high-voltage power sources, and energy harvesting systems [5-6].

Preprints (www.preprints.org) | NOT PEER-REVIEWED | Posted: 17 October 2022 doi:10.20944/preprints202210.0236.v1

However, as a result of lead toxicity, lead-based ferroelectrics are presently a serious environmental hazard. These concerns led to active research on substituting those perovskite-type materials, one ion A or X, with a molecular building unit [7-8].

Hybrid organic-inorganic perovskites (HOIPs) are a recent class of ferroelectric crystalline materials for optoelectronic applications, which are competitive with the inorganic perovskites. These semi-organic ferroelectrics possess many advantages when compared with inorganic ones. For example, they can be synthesized at room temperature, they are more flexible and with lower weight than their inorganic counterparts, and they have remarkable structural variability resulting in high tunable properties. Therefore, they became an attractive topic of research towards their application as piezoelectric and pyroelectric materials that replace inorganic materials [9-12]. Lead-free HOIPs are a recently discovered and highly promising family of perovskites [13-16].

A lead free organic-inorganic perovskite recently discovered is (N-methyl-N'-diazabicyclo[2.2.2]octonium)–ammonium triiodide, MDABCO-NH_4I_3, which has a spontaneous polarization of 22 $\mu C/cm^2$, close to that of barium titanate (which is around 26 $\mu C/cm^2$), a high phase transition temperature at 448 K and several polarization directions. It displays attractive properties for applications in flexible optoelectronic devices [17-18].

The fabrication of structures at the nanoscale has been attracting increased amount of attention because of their size-dependent properties. One-dimensional structures such as nanowires, nanotubes, and nanofibers are the smallest dimensional structures displaying new properties with potential applications in fields such as electronics, photonics, sensing, and energy harvesting.

Electrospinning is a well-established technique for forming micro- and nanoscale fibers with a large surface-to-volume ratio forming mats of several square centimeters area. Electrospun fiber mats are nanostructured multifunctional materials drawn from a precursor polymeric solution blended with functional nanoparticles under very strong static electric fields [19-23].

In addition, the nanofiber anisotropic shape and large surface area ratio contribute to an increase in their mechanical strength and flexibility. In this context, nanoscale ferroelectrics with perovskite structure are a promising research area [9, 24].

One application of functional electrospun fibers is in the harvesting of electrical nanoenergy at low frequencies through the piezoelectric effect, due to the polarization induced by the material deformation [25]. Piezoelectric nanogenerators, usually called PENGs, show potential for powering low-power devices. An example of the use of a semiorganic perovskite as a PENG was reported for the methylammonium lead iodide ($CH_3NH_3PbI_3$) incorporated in PVDF polymer fibers made by electrospinning: an output voltage of approximately 220 mV at 4 Hz, under an applied force of approximately 7.5 N, a maximum output power of 0.8 mW/m^2 was generated [26].

In this work, we demonstrate that piezoactive nanofibers formed by MDABCO-NH_4I_3 perovskite, embedded into three different polymers, namely poly(vinyl chloride) (PVC), polymethyl methacrylate (PMMA), and polyamide (PA66), fabricated by the electrospinning technique, are capable of generating extremely high piezoelectric voltage output and currents, thus acting as lead-free PENG nanogenerators. In particular, for the PVC polymer as the perovskite carrier, MDABCO-NH_4I_3@PVC PENG constructed from electrospun fiber mats are active piezoelectric energy harvesting sources, producing a voltage coefficient g_{eff} = 3.6 VmN^{-1} and an instantaneous power density of 2020 μWm^{-2}, which is two orders of magnitude higher than that delivered by ($CH_3NH_3PbI_3$) in PVDF nanofibers. In addition to the piezoelectric behavior, we also present the luminescence properties of the nanofibers in the UV-vis-NIR and the optical spectra of MDABCO-NH_4I_3 free and embedded in the electrospun fibers. Quite extraordinarily, an extremely intense luminescent band at 325 nm is observed in the nanofibers, with a lower intensity redshifted band having a maximum at 645 nm. It is remarkable that MDABCO-NH_4I_3 nanocrystals inside the fibers show intense solid-state blue luminescence, which has not been reported before for this perovskite. Finally and remarkably, the pyroelectric coefficient of a polycrystalline MDABCO-NH_4I_3 sample and electrospun fibers with incorporated MDABCO-NH_4I_3

 doi:10.20944/preprints202210.0236.v1

nanocrystals is within an order of magnitude of that observed for the well-known bulk ferroelectric triglycine sulfate (TGS).

2. Experimental Section

2.1. Materials and nanofibers preparation

MDABCO-NH_4I_3 was synthesized following the synthetic procedure reported by Yu-Meng You and Ren-Gen Xiong [17]. The precursor (MDABCO)I was synthesized as reported by Kreuer et al. [27]. The MDABCO-NH_4I_3 crystals grown were ground in a mortar and sieved to a size smaller than 40 μm.

All chemicals and solvents were purchased from Sigma-Aldrich and used as received. Poly (methyl methacrylate) (PMMA, Mw 120000) was purchased from Alpha-Aesar. Polyamide 66 (PA66) and Poly(vinyl chloride) (PVC; high molecular weight; density of 1.40 g/ml) were purchased from BDH Chemicals and Janssen, respectively. The 10% polymer solution (w / v) of PMMA was prepared by dissolving the powder in a dichloromethane (DCM)/N,N-dimethylformamide (DMF) solvent blend system (80:20, v / v), with vigorous stirring (400-600 rpm) at room temperature. The 10% (w/v) polymer solution of PA66 was prepared by dissolving the polymer in 5 mL of 1,1,1,3,3,3-hexafluoro-2-propanol (HFP) with vigorous stirring (400-600 rpm) at room temperature. The 10 % precursor electrospinning solution of PVC was prepared by dissolving the pellets in 5 mL of the tetrahydrofuran (THF)/DMF (50:50, v/v) solvent blend system. After complete dissolution, 0.1 g of MDABCO-NH4I3 was incorporated in small portions in a 1: 5 weight ratio and the resulting solution was stirred for several hours under ambient conditions before the electrospinning process. The precursor solution was loaded into a 5 mL syringe with its needle (0.5 mm outer diameter and 0.232mm inner diameter) connected to the anode of a high voltage power supply (Spellmann CZE2000). The nanofibers were produced by a conventional electrospinning technique, previously described [22, 28], with a configuration that tends to produce oriented fiber mats. Briefly, the equipment used has four common components: a high-voltage power supply, a precision syringe pump, a syringe fitted with a metal needle (spinneret) and a drum collector (connected to a motor speed controller). The power supply is connected to both the spinneret and the drum collector. The polymer solution is extruded through the spinneret at a constant flow rate, controlled by the syringe pump. An aluminium foil is attached to the collector in order to collect the prepared fibers. Our electrospinnig apparatus has a vertical geometry.

Polymer nanofibers with embedded MDABCO-NH_4I_3 perovskite using three different polymers were fabricated. Solutions with pure PVC, PMMA, and PA66 polymers were also electrospun and taken as a reference. For the electrospinning of MDABCO-NH_4I_3 containing polymers and reference solutions, a voltage of 18 kV was applied between tip and collector. The flow rate of the solution and the needle-to-collector distance were kept at 0.18-0.30 mL/h and 12 cm, respectively.

The MDABCO-NH4I3 crystals are not stable in open air at room temperature. When the crystals are exposed to air, the perovskite oxidizes, Figures 1(a) and (b). The iodide ions slowly oxidize. The product is molecular iodine, I_2, which darkens the crystals. Previously, to prepare precursor electrospinning solutions, several solvents were tested. In Figure 1 c), it is possible to see that for solvents tetrahydrofuran (THF), methanol, ethanol, and acetone, the intense dark yellow color appears due to the degradation of the perovskite. Hexafluoroisopropanol (HFP) was chosen to prepare the electrospun polymer doped solutions because the solutions remain stable and the perovskite is protected from oxidation for long periods of time after preparation.

Preprints (www.preprints.org) | NOT PEER-REVIEWED | Posted: 17 October 2022 doi:10.20944/preprints202210.0236.v1

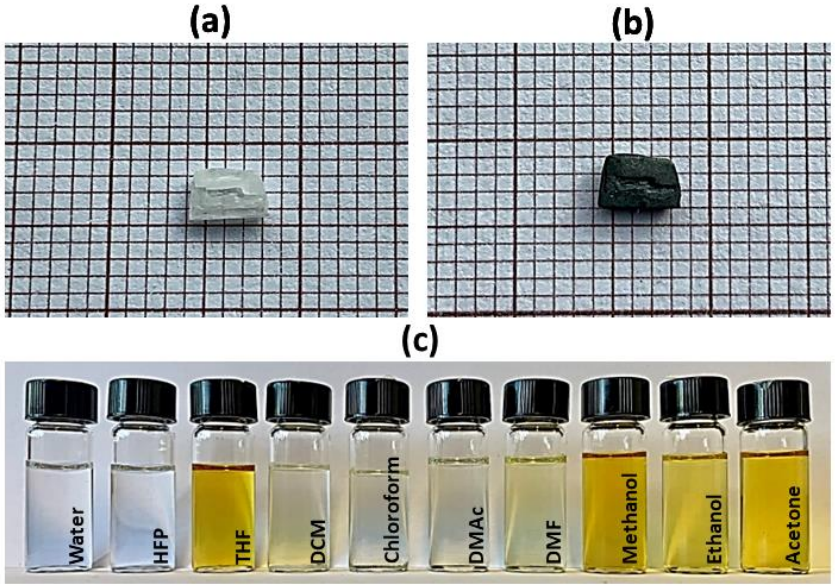

Figure 1. MDABCO-NH_4I_3 perovskite crystal, after several hours **(a)** and after 2 weeks **(b)** of exposure in open air at room temperature. Perovskite solutions in different solvents **(c)**, from left to right: water, hexafluoroisopropanol (HFP), tetrahydrofuran (THF), dichloromethane (DCM), chloroform, dimethylacetamide (DMAc), dimethylformamide (DMF), methanol, ethanol, and acetone.

To make good use of the outstanding crystal properties, we found that, by embedding them into a polymer matrix, the perovskite crystals are protected from oxidation while keeping their optical, piezoelectric, and pyroelectric properties. The perovskite nanocrystals, when embedded into the fibers, are stable for more than half a year because the polymers function as shields protecting the perovskites from oxidation.

PMMA was chosen to prepare the hybrid matrix with MDABCO-NH_4I_3 organic perovskite because it is a biocompatible polymer. PA66, a polymer with a high melting point, around 275-280 ºC, was also chosen because it enables the measurement of the pyroelectric effect on the perovskite nanofibers near their Curie temperature. Finally, PVC polymer was chosen due to its non-toxicity and flexibility, to its strength and high melting point around 220 ºC. The electrospinning process was stable for all the polymers chosen, and the obtained fibers have uniform surfaces and small diameters, demonstrating that there are no crystallites on their surface. The hybrid functional MDABCO-NH_4I_3@PVC, MDABCO-NH4I3@PA66, and MDABCO-NH_4I_3@PMMA nanofibers were further utilized for optical and dielectric characterization, as well as the exemplification of a piezoelectric voltage generator.

2.2. Scanning Electron Microscopy (SEM)

The morphology, size, and shape of MDABCO-NH_4I_3 perovskite nanofibers were studied using a Nova Nano SEM 200 scanning electron microscope operated at an accelerating voltage of 10 kV. Nanofibers were deposited on a silica surface previously covered with a thin film (10 nm thickness) of Au-Pd (80-20 weight %) using a high-resolution sputter cover, 208HR Cressington Company, coupled to a Cressigton MTM-20 high-resolution thickness controller. The diameter range of the nanofibers was measured by SEM images using ImageJ 1.51n image analysis software (NIH, https://imagej.nih.gov/ij/). The average diameter and diameter distribution were determined by measuring 80 random nanofibers from the SEM images, and the fiber diameter distributions fit to a log-normal function.

2.3. X-ray Diffraction and Raman Spectroscopy

Preprints (www.preprints.org) | NOT PEER-REVIEWED | Posted: 17 October 2022 doi:10.20944/preprints202210.0236.v1

The crystallinity and crystallographic orientation of MDABCO-NH_4I_3 inside the fibers was studied by X-ray diffraction. The diffraction pattern using θ–2θ scans was recorded on a Philips PW-1710 X-Ray diffractometer with Cu-Kα radiation of wavelength 1.5406 Å.

Raman spectroscopy was performed on a LabRAM HR Evolution confocal Raman spectrometer (Horiba Scientific, France) using Horiba Scientific's Labspec 6 Spectroscopy Suite software for instrument control, data acquisition and processing. The Raman spectra was obtained using a laser excitation with wavelength 532 nm, at 0.1 % laser intensity, with 30 s acquisition time in a spectral range between 50–3500 cm^{-1}.

2.4. Mechanical Tests

Elastic modulus, stress at yield (at 0.2% offset), tensile strength, and strain at break (at 60% tensile strength) were measured using a universal tensile testing machine Zwick / Roell Z005, following the ASTM D882-02 standard. Several 10x30mm samples, with a gauge length of 16 mm, were tested alongside the oriented fiber direction under a crosshead velocity of 25 mm/min.

2.5. Optical absorption and Photoluminescence

Optical absorption (OA) measurements on a MDABCO-NH4I3 solution were carried out using a Shimadzu UV-3101PC UV–Vis-NIR (Shimadzu Corporation, Kyoto, Japan) spectrophotometer. Photoluminescence spectra were recorded on a Fluorolog 3 spectrofluorimeter (HORIBA Jobin Yvon IBH Ltd., Glasgow, UK). For optical absorption measurements, a 3 mg⁄ml solution of MDABCO-NH_4I_3 was prepared in water. The sample was measured in a quartz cuvette with 1 cm path length. Photoluminescence (PL) spectra acquired using an excitation wavelength of 290 nm, with input and output slits fixed to provide a spectral resolution of 3 nm.

The same spectrophotometer equipped with an integration sphere, Shimadzu ISR-240A, and barium sulfate taken as reference, was used to measure the diffuse reflectance spectrum for the nanofiber array in the wavelength range of 250-800 nm with 1 nm step size. The energy of the band gap, (E_g), was determined using the Kubelka-Munk function given by $[[hvF(R)]^{1/2}]=\alpha(hv-E_g)$, where hv represents the energy of the incident photon, E_g corresponds to the energy of the bad gap, and F(R) is called the Kubelka-Munk function which is directly determined from the total reflectance coefficient of the material (R) through the equation $F(R)=(1-R)^2/2R$ [29,30].

2.6. Dielectric spectroscopy

The dielectric properties of the electrospun fibers with embedded MDABCO-NH_4I_3 inclusions were characterized by impedance spectroscopy, at temperatures of 300-460 K and in the frequency range of 20Hz - 3MHz. The complex permittivity, written as $\varepsilon=\varepsilon'-i\varepsilon''$, where ε and ε'' are the real and imaginary parts, respectively, were calculated from the measured capacitance (C) and loss tangent ($\tan\delta$), using the equations:

$$C = \varepsilon'\varepsilon_0(A/d) \qquad \text{and} \qquad \tan\delta = \varepsilon''/\varepsilon'$$

Here A is the electric contact area and d is the fiber mat thickness. To perform the measurements, the samples formed a parallel plate capacitor and were included in an LCR network. To form the capacitor, the aluminum foil, used as the substrate to collect the fiber mats, was the bottom electrode while the top electrode was the base of cylindrical metal contact, with approximately 10^{-2} m diameter. A Wayne Kerr 6440A precision component analyzer was used together with a dedicated computer and software to acquire the data. Shielded test leads were employed to avoid parasitic impedances due to connecting cables. Temperature-dependent measurements were performed at a rate of 2 ° C / min, using a Polymer Labs PL706 PID controller and furnace.

Pyroelectricity results from the temperature dependence of spontaneous polarization. By changing the temperature, an electric field originated from changes in intrinsic

Preprints (www.preprints.org) | NOT PEER-REVIEWED | Posted: 17 October 2022 doi:10.20944/preprints202210.0236.v1

dipoles is compensated by the surface layer of free charges. The rate of change of the spontaneous polarization $p=dP_s/dT$ is the pyroelectric coefficient. The change in polarization was detected by measuring the pyroelectric current I = A (dPs /dT)(dT /dt), with a Keithley 617 electrometer, where A is the electrode area and dT/dt is the rate of temperature change. The measurements were performed in a capacitor geometry under short-circuit conditions.

2.7. Fabrication of a MDABCO-NH4I3@PVC piezoelectric nanogenerator

A piezoelectric nanogenerator, fabricated using a MDABCO-NH4I3@PVC electrospun fiber mat as the active piezoelectric component, is described in Figure 2. The top and bottom electrodes (area 40x40 mm2) are high-purity copper thin plates. Thin copper wires were attached to the electrodes. The entire system was laminated with 1mm thick cork sheets, to protect and facilitate the handling of the nanogenerator.

Figure 2. Schematic of MDABCO-NH_4I_3@PVC **(a)** Electrospun nanofiber mat sandwiched between two copper electrodes. **(b)** Wires attached to the electrodes. **(c)** The complete laminated system with thin cork sheets.

3. Results and Discussion

3.1. Electrospun fibers

The perovskite polymer solutions obtained remain stable with no color change for several weeks, Figure 3 a). The electrospinning process is stable with no current fluctuations and a steady flow of the polymer solution at the tip of the needle. The fabricated fibers are very flexible (inset) show no 'beads' or crystallites grown on their surface, have a white appearance, and are flexible, Figure 3 b).

Figure 3. Perovskite polymeric solution **(a)** and MDABCO-NH4I3 @ PVC electrospun nanofiber mat **(b)** the inset shows a fiber mat folded around a cylindrical stick, demonstrating the flexibility of the fibers.

3.2. Fibers morphology and crystallinity

Figure 4 shows scanning electron microscopy (SEM) images of the fibers prepared with different polymers with embedded MDABCO-NH_4I_3 perovskite, along with the corresponding histograms of the diameter sizes. The diameter distributions are observed to follow a log-normal dependence, with average values from 200 to 605 nm.

Preprints (www.preprints.org) | NOT PEER-REVIEWED | Posted: 17 October 2022 doi:10.20944/preprints202210.0236.v1

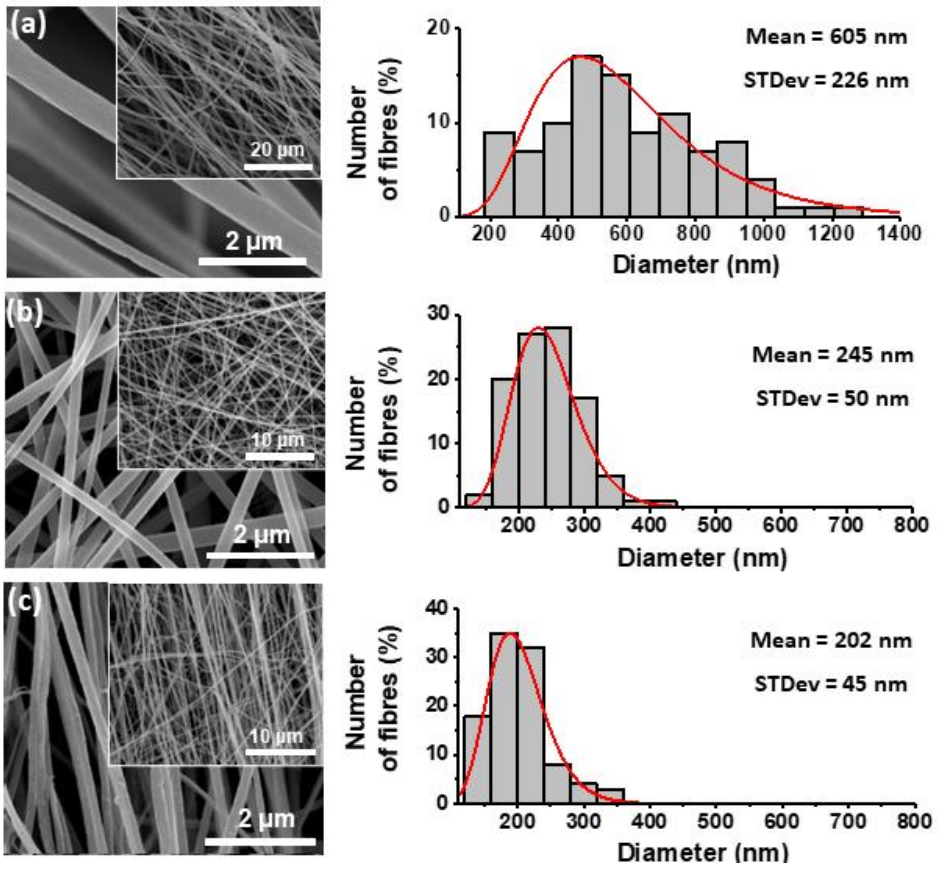

Figure 4. SEM images at magnification levels of 10,000x and 50,000x and respective fiber diameter distribution histograms for PMMA **(a)**, PA66 **(b)** and PVC **(c)** nanofibers with embedded MDABCO-NH_4I_3 perovskite crystals. The red curves indicate logarithmic normal distributions using the mean and standard deviations of each set of fibers.

X-ray diffraction patterns obtained from the doped fibers are shown in Figure 5 b) to d) and compared to the correspondent pattern for the polycrystalline synthesized MDABCO-NH_4I_3 perovskite, Figure 5 a), where all the Bragg peaks were indexed using the published crystal structure (cif file 1836322) [17]. We conclude that for all of the fibers the embedded perovskite is in its crystalline ferroelectric phase and is randomly oriented inside the different polymer matrices. The crystallite size of the perovskites was evaluated for each polymer, from fitting with the Debye-Scherrer equation the two most intense Bragg reflections $(11\bar{1})$ and (200), see SI, Figures SI1a-SI1c. The average size varies between 60 and 85 nm, as indicated in Table 1.

Table 1. Average crystallite size of MDABCO-NH4I3 perovskite crystals embedded in electrospun fibers.

MDABCO-NH_4I_3 in	size (nm)
PVC	62 ± 12
PMMA	77 ± 06
PA66	83 ± 17

Preprints (www.preprints.org) | NOT PEER-REVIEWED | Posted: 17 October 2022 doi:10.20944/preprints202210.0236.v1

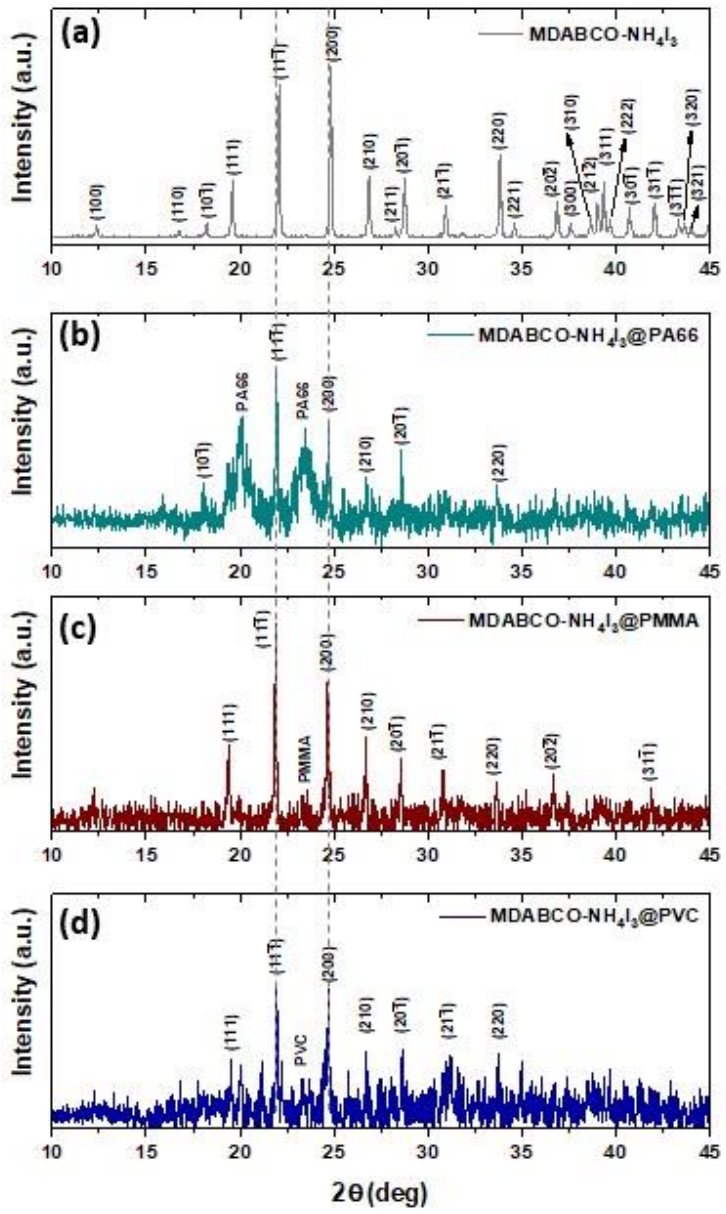

Figure 5. (a) Synthesized perovskite crystals with all Bragg peaks indexed from the published CIF file 1836322 [17]. X-ray patterns of PA66 **(b)**, PMMA **(c),** and PVC **(d)** nanofibers with embedded MDABCO-NH_4I_3 perovskite crystals, between 10º and 45º.

3.3. Optical Absorption and Luminescence

The reflectance spectra of a MDABCO-NH_4I_3 pellet and MDABCO-NH_4I_3@PVC nanofibers show two absorption bands with maximum at wavelengths of 297 nm and 365 nm and 298 nm and 367 nm, respectively, as shown in Figure 6. PVC electrospun fibers are highly transparent in all UV-Vis spectra. The energy band gap, E_g, calculated for pellet crystals and nanofibers, from the intersection with the energy axis of a linear Kubelka-Munk function, are respectively 4.760 eV and 4.824 eV as indicated in the insets of Figure 6. These values are in excellent agreement with 4.950 eV as previously reported [31]. Similar reflectance spectra measured for MDABCO-NH_4I_3@PMMA and MDABCO-NH_4I_3@PA66 nanofibers are shown in SI Figure SI2.

Preprints (www.preprints.org) | NOT PEER-REVIEWED | Posted: 17 October 2022 doi:10.20944/preprints202210.0236.v1

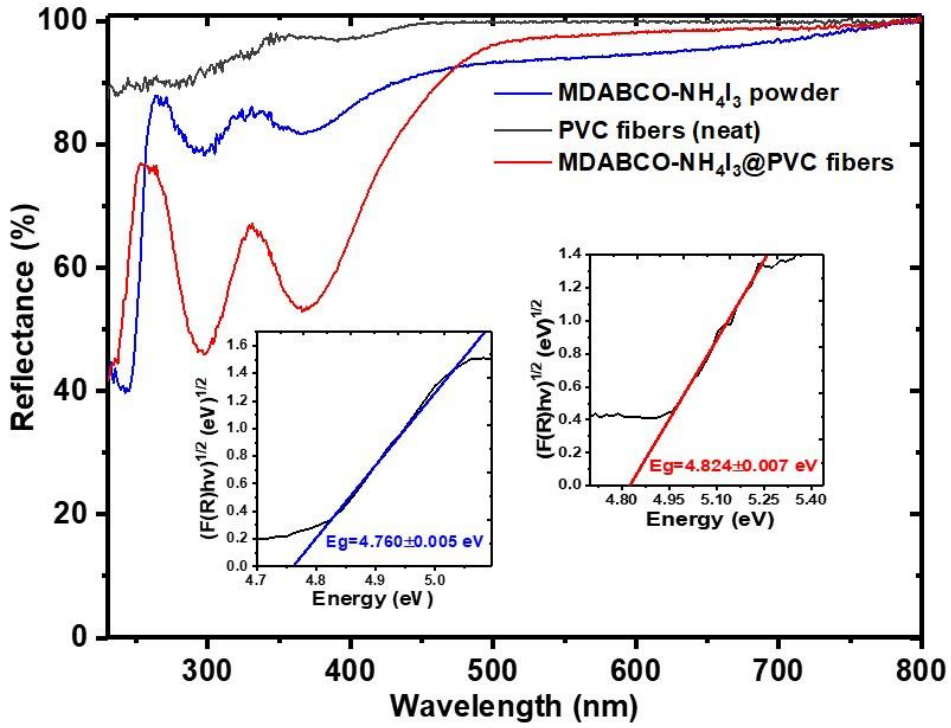

Figure 6. UV–vis reflectance of MDABCO-NH_4I_3 powder and electrospun PVC fibers with MDABCO-NH_4I_3 nanocrystals. The inset shows the Kubelka-Munk function indicating a band gap energy of 4.760 and 4.824 eV for powder and fibers, respectively.

At high wavelengths (low photon energies), both free perovskite and electrospun fibers containing the perovskite are highly transparent, and the absorption becomes stronger at the band-gap energy. High transparency in the visible and near infrared-red regions of the optical spectra is important for linear and nonlinear optical applications [32,33].

Figure 7 shows the OA of a water solution MDABCO-NH4I3 and the emission of PL from the same solution and also the dissolved MDABCO-NH_4I_3@PVC fibers, for excitation at 289 nm. For the MDABCO-NH_4I_3 water solution, the PL emission shows one intense band in the UV with a maximum at 325 nm, a slightly lower intense band in the blue with a maximum at 395 nm and a redshifted band with a maximum at 645 nm. For nanofibers (the solvent used dissolves only the polymer and not the perovskite nanocrystals) an extremely intense PL band at 325 nm and a less intense redshifted band with maximum at 645 nm are observed. It is remarkable that MDABCO-NH_4I_3 nanocrystals inside the fibers show intense solid-state UV and blue luminescence, which is reported in this study for the first time for MDABCO-NH_4I_3 perovskite nanocrystals. The reflectance spectra of a MDABCO-NH_4I_3 pellet and MDABCO-NH_4I_3@PVC nanofibers, show two absorption bands with maxima at the wavelengths of 297 nm and 365 nm and 298 nm and 367 nm, respectively, as shown in Figure 6. PVC electrospun fibers are highly transparent in all UV-Vis spectra. The energy band gap, E_g, calculated for pellet crystals and nanofibers, from the intersection with the energy axis of a linear Kubelka-Munk function, are respectively 4.760 eV and 4.824 eV as indicated in the insets of Figure 6. These values are in excellent agreement with 4.950 eV as previously reported [31]. Similar reflectance spectra measured for MDABCO-NH_4I_3@PMMA and MDABCO-NH_4I_3@PA66 nanofibers are shown in SI Figure SI2.

Preprints (www.preprints.org) | NOT PEER-REVIEWED | Posted: 17 October 2022 doi:10.20944/preprints202210.0236.v1

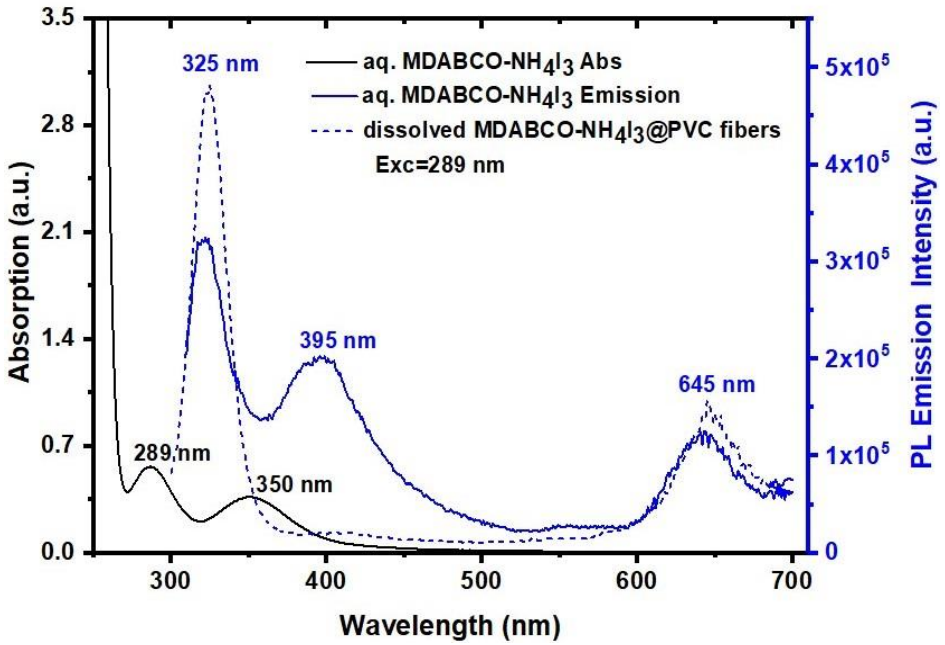

Figure 7. Optical absorption and photoluminescence emission of MDABCO-NH_4I_3 aqueous solution (3 mg/mL) and MDABCO-NH_4I_3@PVC nanofibers dissolved in tetrahydrofuran.

3.4. Dielectric Measurements

The complex dielectric permittivity measured on a polycrystalline sample of MDABCO-NH4I3 (pellet), between 300 K and 470 K as a function of frequency, shows that the ferroelectric-paraelectric phase transition occurs at 440 K, Figure 8 a) and b). As expected for a proper ferroelectric system, the real part of the permittivity increases with decreasing frequency, reaching the Curie transition temperature 42500 (at 20 Hz). Quite extraordinarily, this very high value of ε′, measured on a pellet, is 3000 times higher than that reported for an oriented single crystal, which was 14068 at the same frequency of 20 Hz [17]. This indicates the high purity of our synthesized MDABCO-NH_4I_3 crystals.

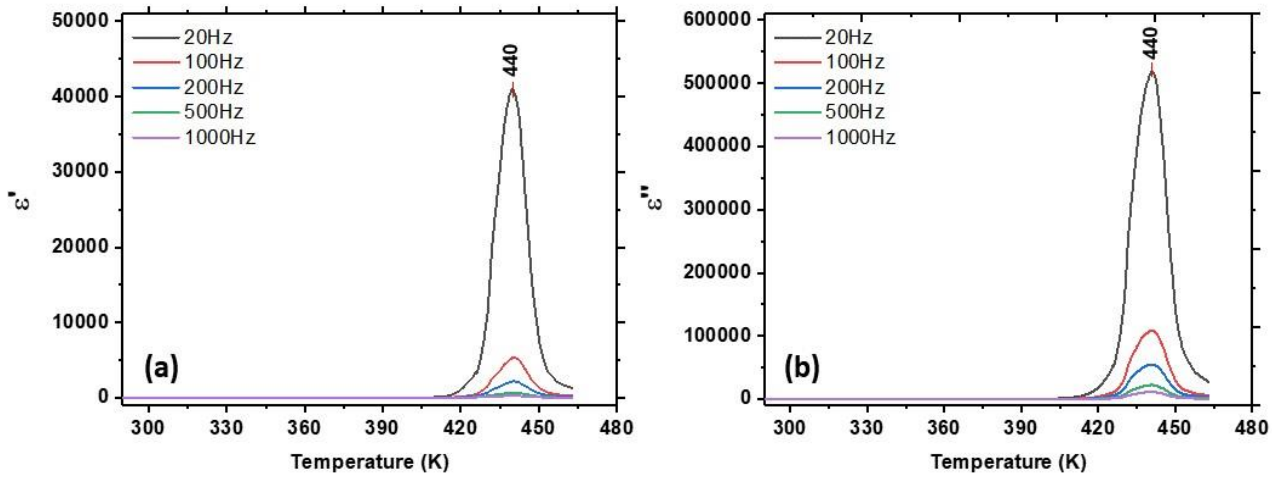

Figure 8. Dielectric permittivity of a MDABCO-NH_4I_3 polycrystalline sample showing its **(a)** real and **(b)** imaginary parts as functions of temperature and frequency. The ferroelectric-paraelectric phase transition occurs at 440 K.

The real and imaginary parts of the dielectric permittivity were also measured on a MDABCO-NH_4I_3@PA66 electrospun fiber mat in the same temperature and frequency range, as shown in Figure 9 a) and b) for frequencies below 1000 Hz. The transition is perceptible at 462 K, a little above the temperature of 440 K measured for a polycrystalline

Preprints (www.preprints.org) | NOT PEER-REVIEWED | Posted: 17 October 2022 doi:10.20944/preprints202210.0236.v1

perovskite (Figure 8). This results from the fact that the nanocrystals are immersed in the polymer matrix, making it necessary to go higher in temperature for the dispersed nanocrystals to make the ferroelectric-paraelectric transition temperature. It also indicates a diffuse character of the phase transition, induced by the small size of the MDABCO-NH_4I_3 nanocrystals, embedded in the polymer matrix.

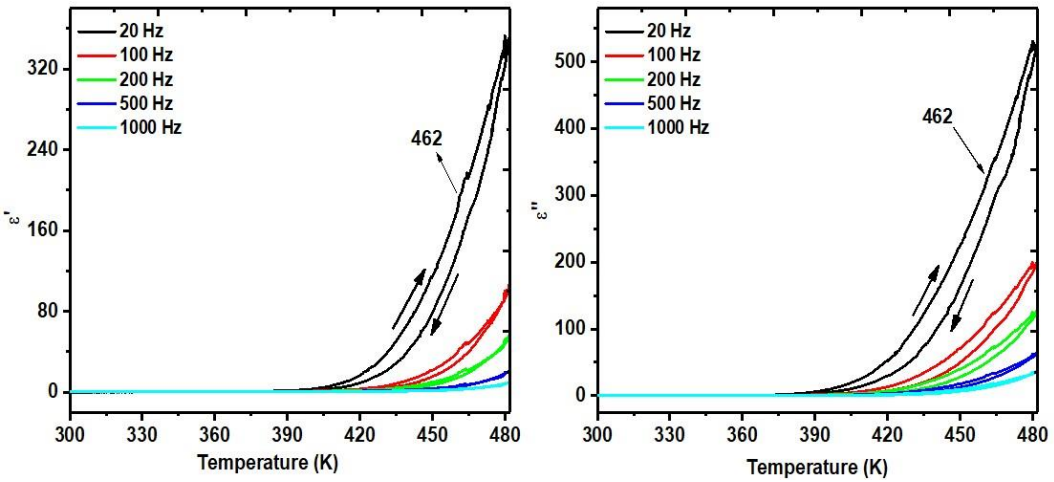

Figure 9. Dielectric permittivity of MDABCO-NH_4I_3 nanocrystals embedded in electrospun fibers, MDABCO-NH_4I_3@PA66a showing the ferroelectric-paraelectric phase transition at 462 K. The arrows indicate the heating and cooling dielectric cycle.

3.5. Pyroelectricity in fibers

In this work, we report for the first time the measurement of the pyroelectric coefficient of polycrystalline MDABCO-NH_4I_3 perovskite (a pellet) and of nanocrystals embedded in electrospun fibers of PA66, that is, MDABCO-NH_4I_3@PA66. Note that PA66 is the only polymer that allowed the pyroelectric measurement to be carried out, since both PMMA and PVC melt before the perovskite phase-transition temperature is achieved. The measured coefficients, as a function of temperature, are shown in Figure 10 for a fiber mat.

Extraordinarily, the pyroelectric coefficient of the MDABCO-NH_4I_3 nanocrystals increases to a very high value of 194×10^{-6} $Cm^{-2}k^{-1}$ achieved at 483 K, which is slightly above the Curie transition temperature value obtained for measurements of dielectric permittivity. This indicates a diffuse phase transition, which is expected to occur for nanocrystals randomly oriented inside a polymer matrix. The pyroelectric coefficient value obtained is within the same order of magnitude as that reported for the state-of-the-art semiorganic ferroelectric triglycine sulfate (TGS) single crystal, reported to be 306×10^{-6} $Cm^{-2}k^{-1}$ [34].

Preprints (www.preprints.org) | NOT PEER-REVIEWED | Posted: 17 October 2022 doi:10.20944/preprints202210.0236.v1

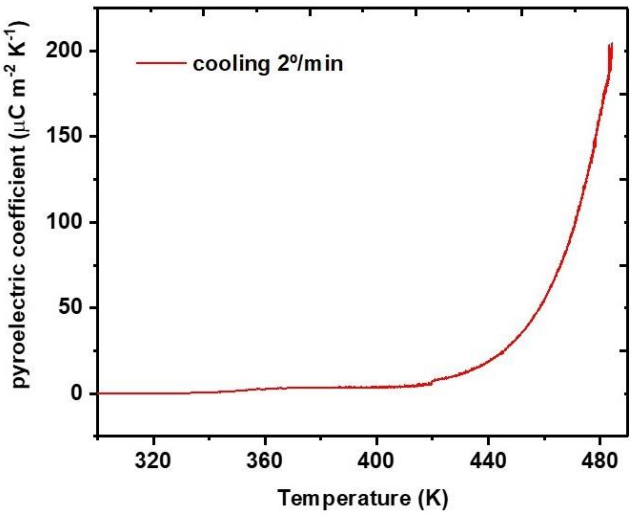

Figure 10. Pyroelectric coefficient as a function of temperature of MDABCO-NH_4I_3@PA66 nanofibers, measured on cooling from the Curie transition temperature.

3.6. Piezoelectric voltage and effective piezoelectric coefficients in fibers

The behavior of the electrospun nanofiber mats fabricated from MDABCO-NH_4I_3@PA66, MDABCO-NH_4I_3@PMMA and MDABCO-NH4I3@PVC is now studied is now studied as a piezoelectric energy generator. The generated open-circuit voltage, *Voc*, and short-circuit currents, *Isc*, are shown in Figure 11 as functions of the external forces applied. In SI, Figure SI6, the piezoelectric current generated by a MDABCO-NH_4I_3@PA66 fiber mat is shown. There is a linear relationship between the output electric current generated and the applied external forces, as expected for a piezoelectric material. For the MDABCO-NH4I3 @ PVC fiber mat, Figure SI7 shows the piezoelectric current generated during a time interval of 130 s under a periodical force applied with 4.5 N at a frequency of 3 Hz, as well as for frequencies between 1Hz and 12 Hz.

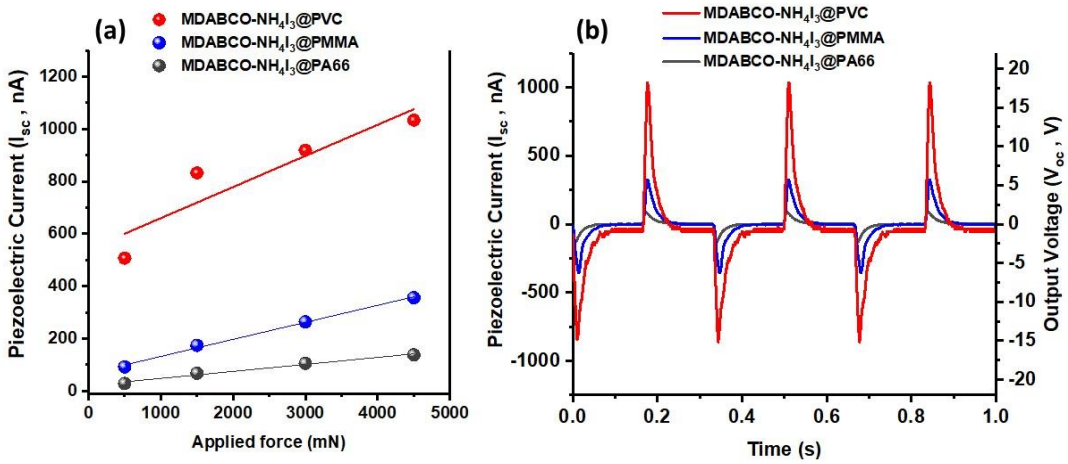

Figure 11. (a) Piezoelectric current as a function of the applied forces and **(b)** Output voltage and current as a function of time from MDABCO-NH_4I_3 incorporated into different electrospun polymer nanofibers.

The MDABCO-NH_4I_3@PVC nanofibers are very flexible and show a tensile strength and Young modulus of approximately 4.0 MPa and 58 MPa, respectively, as shown in Figure SI8. Flexibility and high Young modulus are important characteristics for the performance of a fiber mat as a nanogenerator because they will increase its capacity to last for longer times under applied external force.

Preprints (www.preprints.org) | NOT PEER-REVIEWED | Posted: 17 October 2022 doi:10.20944/preprints202210.0236.v1

For a frequency of 3Hz and compression stress of 11 kPa, V_{oc} reaches 16.5 V for the PENG formed by the MDABCO-NH_4I_3@PVC nanofiber mat. For MDABCO-NH_4I_3@PMMA and MDABCO-NH_4I_3@PA66, V_{oc} reaches respectively 6.1 V and 2.0 V. Low frequencies such as 3Hz are those that enable the generator to return to its original microscopic configuration before the next force is applied.

The charge generated by a piezoelectric mat, calculated from Q=∫Idt (C), resultsin a charge of 786 pC for the MDABCO-NH_4I_3@PVC mat considering a material response time of the order of 10^{-3} s and the maximum I_{sc} obtained of 786 nA. For MDABCO-NH_4I_3@PMMA and MDABCO-NH_4I_3@PA66 fiber mats, the charges generated are, respectively, 288 pC and 95 pC. We may now calculate the effective piezoelectric coefficient, given by d_{eff} = Q/F (pCN^{-1}) for the three nanofiber mats under a periodical force applied at 4.5 N. These are 175 pCN^{-1}, 64 pCN^{-1} and 21 pCN^{-1}, respectively, for MDABCO-NH_4I_3@PVC, MDABCO-NH_4I_3@PMMA and MDABCO-NH4I3@PA66. The piezoelectric coefficient reported for a single MDABCO-NH4I3 crystal is d_{33}=14 pCN^{-1} along [1 1 1] [17]. Therefore, the piezoelectric coefficient for the hybrid system formed by MDABCO-NH_4I_3 nanocrystals embedded in PVC fibers is one order of magnitude higher. Note that for this hybrid perovskite PENG, there is a small contribution from the piezoelectric polymer which is piezoelectric (d_{31}~1.5 pCN^{-1}) [35]. The present result is consistent with the very high effective piezoelectric coefficient displayed by electrospun fibers incorporated with active organic piezoelectric materials, which has been previously reported for nonlinear optical organic crystal derivatives of nanocrystalline push-pull nitroaniline molecules and diphenylalanine dipeptides, when embedded in nano and microfibers fabricated by the electrospinning technique [36-38].

It is also important to calculate the peak power density, P = I_{sc}/A (μWm^{-2}) (A is the electrodes area) delivered by the MDABCO-NH4I3 @ PVC nanofiber mat, which amounts to 1960 μWm^{-2}, two orders of magnitude higher than that reported for the methylammonium lead iodide ($CH_3NH_3PbI_3$) embedded into poly(vinylfluoride(PVDF) nanofibers, reported to be 12 μWm^{-2} for R_l = 10 MΩ [26]. Furthermore, our MDABCO-NH_4I_3@PVC piezoelectric generator is capable of delivering a peak power density with magnitude similar to that achieved for electrically poled MDABCO-NH4I3 films deposited on a polyimide substrate after a preheating treatment up to 140 ° C. Here, the piezoelectric generator delivered a peak power density of 2000 μWm^{-2} under an R_l = 250 MΩ [39]. Therefore, our electrospun-doped fiber mat can achieve a high peak power density without the need of electrical polling or previous heating treatment, which is very advantageous.

In the present work, we demonstrate that incorporating the organic lead-free perovskite MDABCO-NH4I3 into electrospun PVC fibers, processed at room temperature without poling, is an easy and straightforward way to fabricate piezoelectric generators using lead-free perovskite nanocrystals as active materials. Moreover, the piezoelectric voltage coefficient is defined as

$$g_{eff} = d_{eff}/(\varepsilon' \varepsilon_0) \text{ VmN}^{-1}$$

which is an important quantity for quantifying the performance of a material for integration as a piezoelectric sensor, was calculated for our electrospun fiber mats. For MDABCO-NH_4I_3@PVC, ε′= 50 at 20 Hz and g_{eff} = 3.6 VmN^{-1}. This extremely high piezoelectric voltage coefficient, which is one order of magnitude higher than that displayed by a polyvinylidene fluoride (PVDF) polymer thin film for which g_{eff} = 0.29 VmN^{-1}[40,41] and six times higher than that exhibited by the layered lead perovskite (4-aminotetrahydropyran)$_2PbBr_4$, which was reported to be g_{eff} = 0.67 VmN^{-1} [9].

4. Conclusions

In this study, we show that the organic ferroelectric perovskite N-methyl-N'-diazabicyclo[2.2.2]octonium)–ammonium triiodide (MDABCO-NH_4I_3) incorporated into electrospun fibers of three different polymers, processed at room temperature and without poling, can generate output voltages ranging from 2 V to ~17 V, using lead-free perovskite

 doi:10.20944/preprints202210.0236.v1

nanocrystals as active piezoelectric materials. In particular, we show that MDABCO-NH_4I_3 embedded in PVC fibers displays an effective piezoelectric voltage coefficient as high as g_{eff} =3.6 VmN^{-1}.

A piezoelectric nanogenerator is demonstrated, fabricated using a MDABCO-NH_4I_3@PVC electrospun fiber mat as the active piezoelectric component. Electrospun fibers exhibit intense blue photoluminescence at 325 nm, emitted by the embedded perovskite nanocrystals. Importantly, the pyroelectric coefficient of MDABCO-NH_4I_3 nanocrystals increases to the very high value of 194×10^{-6} $Cm^{-2}k^{-1}$ achieved at the ferroelectric-paraelectric transition. This pyroelectric coefficient has a magnitude within the same order as that reported for a semi-organic ferroelectric triglycine sulfate (TGS) single crystal. Importantly, the nanocrystals maintain their optical, piezoelectric, and pyroelectric properties for long periods, when embedded into electrospun fibers, inhibiting the perovskite oxixation promoted by the polymer matrix.

Supplementary Materials: The following supporting information can be downloaded at: www.mdpi.com/xxx/s1, Table SI1: Fit parameter values correspondent to Bragg reflection (11$\bar{1}$); Table SI2: Fit parameter values correspondent to Bragg reflection (200); Figure SI1: Asymmetric pseudo-Voigt fits; Figure SI2: UV–vis reflectance; Figure SI3: DSC spectra ; Figure SI4: Raman spectra; Figure SI5: FTIR-ATR spectra; Figure SI6: Piezoelectric current; Figure SI7: piezoelectric current generated for frequencies between 1Hz and 12Hz; Figure SI8: Elastic modulus, stress at yield, tensile strength and strain at break.

Author Contributions: Conceptualization, R.B. and E.G.; investigation, R.B., G. M., B.A., B.S., J.O., P.R., A.M., C.C. and M.B.; writing—original draft preparation, R.B. and E.G.; writing—review and editing, R.B., E.G., B.A., M.B.; supervision, R.B. and E.G.; project administration, R.B. and E.G.; funding acquisition, R.B. and E.G. All authors have read and agreed to the published version of the manuscript.

Institutional Review Board Statement: This study did not involve humans or animals.

Informed Consent Statement: This study did not involve humans or animals.

Acknowledgments: We acknowledge FEDER (European Fund for Regional Development)-COMPETE-QREN-EU for financial support through the Physics Centers of the Universities of Minho and Porto (Ref. UID/FIS/04650/2013 and UID/FIS/04650/2019). Part of this work was funded by national funds (OE), through FCT − Fundação para a Ciência e a Tecnologia, I.P., in the scope of the framework contract foreseen in the numbers 4, 5, and 6 of the article 23, of the Decree-Law 57/2016, of August 29, changed by Law 57/2017, of July 19.

Conflicts of Interest: The authors declare no conflict of interest.

Graphical abstract

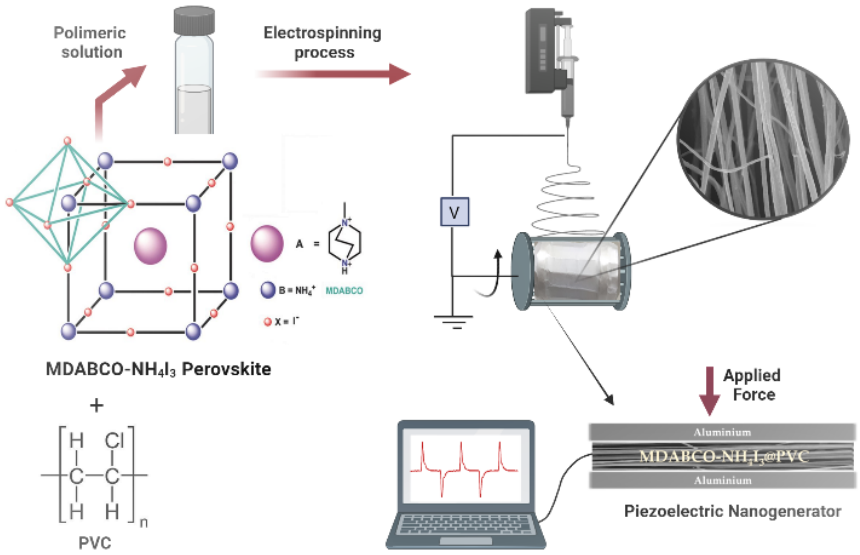

References

1. Valasek, J. Properties of Rochelle Salt Related to the Piezo-electric Effect. *Phys. Rev.* **1922**, *20*, 639-664, doi:10.1103/PhysRev.20.639.
2. Valasek, J. Piezo-Electric and Allied Phenomena in Rochelle Salt. *Phys. Rev.* **1921**, *17*, 475-481, doi:10.1103/PhysRev.17.475.
3. Lines, M.E.; Glass, A.M. *Principles and Applications of Ferroelectrics and Related Materials*; Oxford University Press: Oxford, 2001; p. 694.
4. Scott James, F.; Paz de Araujo Carlos, A. Ferroelectric Memories. *Science* **1989**, *246*, 1400-1405, doi:10.1126/science.246.4936.1400.
5. Zhao, Z.; Dai, Y.; Dou, S.X.; Liang, J. Flexible nanogenerators for wearable electronic applications based on piezoelectric materials. *Mater. Today Energy* **2021**, *20*, 100690, doi:https://doi.org/10.1016/j.mtener.2021.100690.
6. Sezer, N.; Koç, M. A comprehensive review on the state-of-the-art of piezoelectric energy harvesting. *Nano Energy* **2021**, *80*, 105567, doi:https://doi.org/10.1016/j.nanoen.2020.105567.
7. Cross, E. Lead-free at last. *Nature* **2004**, *432*, 24-25, doi:10.1038/nature03142.
8. Saito, Y.; Takao, H.; Tani, T.; Nonoyama, T.; Takatori, K.; Homma, T.; Nagaya, T.; Nakamura, M. Lead-free piezoceramics. *Nature* **2004**, *432*, 84-87, doi:10.1038/nature03028.
9. Chen, X.-G.; Song, X.-J.; Zhang, Z.-X.; Li, P.-F.; Ge, J.-Z.; Tang, Y.-Y.; Gao, J.-X.; Zhang, W.-Y.; Fu, D.-W.; You, Y.-M.; et al. Two-Dimensional Layered Perovskite Ferroelectric with Giant Piezoelectric Voltage Coefficient. *J. Am. Chem. Soc.* **2020**, *142*, 1077-1082, doi:10.1021/jacs.9b12368.
10. Guo, T.-M.; Gong, Y.-J.; Li, Z.-G.; Liu, Y.-M.; Li, W.; Li, Z.-Y.; Bu, X.-H. A New Hybrid Lead-Free Metal Halide Piezoelectric for Energy Harvesting and Human Motion Sensing. *Small* **2022**, *18*, 2103829, doi:https://doi.org/10.1002/smll.202103829.
11. Zhang, H.-Y.; Tang, Y.-Y.; Shi, P.-P.; Xiong, R.-G. Toward the Targeted Design of Molecular Ferroelectrics: Modifying Molecular Symmetries and Homochirality. *Accounts Chem. Res.* **2019**, *52*, 1928-1938, doi:10.1021/acs.accounts.8b00677.
12. Li, W.; Wang, Z.; Deschler, F.; Gao, S.; Friend, R.H.; Cheetham, A.K. Chemically diverse and multifunctional hybrid organic–inorganic perovskites. *Nat. Rev. Mater.* **2017**, *2*, 16099, doi:10.1038/natrevmats.2016.99.
13. Song, X.; Hodes, G.; Zhao, K.; Liu, S. Metal-Free Organic Halide Perovskite: A New Class for Next Optoelectronic Generation Devices. *Adv. Energy Mater.* **2021**, *11*, 2003331, doi:https://doi.org/10.1002/aenm.202003331.
14. Chu, L.-L.; Zhang, T.; Zhang, W.-Y.; Shi, P.-P.; Gao, J.-X.; Ye, Q.; Fu, D.-W. Three-Dimensional Metal-Free Molecular Perovskite with a Thermally Induced Switchable Dielectric Response. *J. Phys. Chem. Lett.* **2020**, *11*, 1668-1674, doi:10.1021/acs.jpclett.9b03556.
15. You, Y.-M.; Liao, W.-Q.; Zhao, D.; Ye, H.-Y.; Zhang, Y.; Zhou, Q.; Niu, X.; Wang, J.; Li, P.-F.; Fu, D.-W.; et al. An organic-inorganic perovskite ferroelectric with large piezoelectric response. *Science* **2017**, *357*, 306-309, doi:10.1126/science.aai8535.
16. Saparov, B.; Mitzi, D.B. Organic–Inorganic Perovskites: Structural Versatility for Functional Materials Design. *Chem. Rev.* **2016**, *116*, 4558-4596, doi:10.1021/acs.chemrev.5b00715.
17. Ye, H.-Y.; Tang, Y.-Y.; Li, P.-F.; Liao, W.-Q.; Gao, J.-X.; Hua, X.-N.; Cai, H.; Shi, P.-P.; You, Y.-M.; Xiong, R.-G. Metal-free three-dimensional perovskite ferroelectrics. *Science* **2018**, *361*, 151-155, doi:10.1126/science.aas9330.

18. Wang, H.; Liu, H.; Zhang, Z.; Liu, Z.; Lv, Z.; Li, T.; Ju, W.; Li, H.; Cai, X.; Han, H. Large piezoelectric response in a family of metal-free perovskite ferroelectric compounds from first-principles calculations. *npj Comput. Mater.* **2019**, *5*, 17, doi:10.1038/s41524-019-0157-4.
19. Doshi, J.; Reneker, D.H. Electrospinning process and applications of electrospun fibers. *J. Electrostat.* **1995**, *35*, 151-160, doi:https://doi.org/10.1016/0304-3886(95)00041-8.
20. Reneker, D.H.; Chun, I. Nanometre diameter fibres of polymer, produced by electrospinning. *Nanotechnology* **1996**, *7*, 216 - 223.
21. Ramakrishna, S.; Fujihara, K.; Teo, W.-E.; Yong, T.; Ma, Z.; Ramaseshan, R. Electrospun nanofibers: solving global issues. *Materials Today* **2006**, *9*, 40-50, doi:https://doi.org/10.1016/S1369-7021(06)71389-X.
22. Isakov, D.V.; de Matos Gomes, E.; Vieira, L.G.; Dekola, T.; Belsley, M.S.; Almeida, B.G. Oriented single-crystal-like molecular arrangement of optically nonlinear 2-methyl-4-nitroaniline in electrospun nanofibers. *ACS Nano* **2011**, *5*, 73-78.
23. Richard-Lacroix, M.; Pellerin, C. Molecular Orientation in Electrospun Fibers: From Mats to Single Fibers. *Macromolecules* **2013**, *46*, 9473-9493, doi:10.1021/ma401681m.
24. Rørvik, P.M.; Grande, T.; Einarsrud, M.-A. One-Dimensional Nanostructures of Ferroelectric Perovskites. *Adv. Mater.* **2011**, *23*, 4007-4034, doi:https://doi.org/10.1002/adma.201004676.
25. Isakov, D.; de Matos Gomes, E.; Almeida, B.; Kholkin, A.L.; Zelenovskiy, P.; Neradovskiy, M.; Shur, V.Y. Energy harvesting from nanofibers of hybrid organic ferroelectric dabcoHReO4. *Appl. Phys. Lett.* **2014**, *104*, 032907, doi:10.1063/1.4862437.
26. Sultana, A.; Ghosh, S.K.; Alam, M.M.; Sadhukhan, P.; Roy, K.; Xie, M.; Bowen, C.R.; Sarkar, S.; Das, S.; Middya, T.R.; et al. Methylammonium Lead Iodide Incorporated Poly(vinylidene fluoride) Nanofibers for Flexible Piezoelectric–Pyroelectric Nanogenerator. *ACS Appl. Mater. Inter.* **2019**, *11*, 27279-27287, doi:10.1021/acsami.9b04812.
27. Marino, M.G.; Kreuer, K.D. Alkaline Stability of Quaternary Ammonium Cations for Alkaline Fuel Cell Membranes and Ionic Liquids. *ChemSusChem* **2015**, *8*, 513-523, doi:10.1002/cssc.201403022.
28. Sá, P.; Barbosa, J.; Bdikin, I.; Almeida, B.; Rolo, A.G.; Gomes, E.d.M.; Belsley, M.; Kholkin, A.L.; Isakov, D. Ferroelectric characterization of aligned barium titanate nanofibres. *J. Phys. D: Appl. Phys.* **2013**, *46*, 105304, doi:10.1088/0022-3727/46/10/105304.
29. Kubelka, P. New Contributions to the Optics of Intensely Light-Scattering Materials. Part I. *J. Opt. Soc. Am.* **1948**, *38*, 448-457, doi:10.1364/JOSA.38.000448.
30. Makuła, P.; Pacia, M.; Macyk, W. How To Correctly Determine the Band Gap Energy of Modified Semiconductor Photocatalysts Based on UV–Vis Spectra. *J. Phys. Chem. Lett.* **2018**, *9*, 6814-6817, doi:10.1021/acs.jpclett.8b02892.
31. Song, X.; Li, Q.; Han, J.; Ma, C.; Xu, Z.; Li, H.; Wang, P.; Yang, Z.; Cui, Q.; Gao, L.; et al. Highly Luminescent Metal-Free Perovskite Single Crystal for Biocompatible X-Ray Detector to Attain Highest Sensitivity. *Adv. Mater.* **2021**, *33*, 2102190, doi:https://doi.org/10.1002/adma.202102190.
32. Kasel, T.W.; Deng, Z.; Mroz, A.M.; Hendon, C.H.; Butler, K.T.; Canepa, P. Metal-free perovskites for non linear optical materials. *Chem. Sci.* **2019**, *10*, 8187-8194, doi:10.1039/C9SC03378E.
33. Sirbu, D.; Tsui, H.C.L.; Alsaif, N.; Iglesias-Porras, S.; Zhang, Y.; Wang, M.; Liu, M.; Peacock, A.C.; Docampo, P.; Healy, N. Wide-Band-Gap Metal-Free Perovskite for Third-Order Nonlinear Optics. *ACS Photonics* **2021**, *8*, 2450-2458, doi:10.1021/acsphotonics.1c00687.
34. Ghane-Motlagh, R.; Kroener, M.; Goldschmidtboeing, F.; Danilewsky, A.N.; Woias, P. A dynamic method for the measurement of pyroelectric properties of materials. *Smart Mater. Struct.* **2018**, *27*, doi:10.1088/1361-665x/aac0b3.
35. Bharti, V.; Kaura, T.; Nath, R. Improved piezoelectricity in solvent-cast PVC films. *IEEE Trans. Dielectr. Electr. Insul.* **1995**, *2*, 1106-1110, doi:10.1109/TDEI.1995.8881940.
36. Baptista, R.M.F.; Lopes, P.E.; Rodrigues, A.R.O.; Cerca, N.; Belsley, M.S.; de Matos Gomes, E. Self-assembly of Boc-p-nitro-l-phenylalanyl-p-nitro-l-phenylalanine and Boc-l-phenylalanyl-l-tyrosine in solution and into piezoelectric electrospun fibers. *Mater. Adv.* **2022**, *3*, 2934-2944, doi:10.1039/D1MA01022K.
37. Baptista, R.M.F.; de Matos Gomes, E.; Raposo, M.M.M.; Costa, S.P.G.; Lopes, P.E.; Almeida, B.; Belsley, M.S. Self-assembly of dipeptide Boc-diphenylalanine nanotubes inside electrospun polymeric fibers with strong piezoelectric response. *Nanoscale Adv.* **2019**, *1*, 4339-4346, doi:10.1039/C9NA00464E.
38. Bernardo, C.R.; Baptista, R.M.F.; de Matos Gomes, E.; Lopes, P.E.; Raposo, M.M.M.; Costa, S.P.G.; Belsley, M.S. Anisotropic PCL nanofibers embedded with nonlinear nanocrystals as strong generators of polarized second harmonic light and piezoelectric currents. *Nanoscale Adv.* **2020**, *2*, 1206-1213, doi:10.1039/C9NA00687G.
39. Wu, H.-S.; Wei, S.-M.; Chen, S.-W.; Pan, H.-C.; Pan, W.-P.; Huang, S.-M.; Tsai, M.-L.; Yang, P.-K. Metal-Free Perovskite Piezoelectric Nanogenerators for Human–Machine Interfaces and Self-Powered Electrical Stimulation Applications. *Adv. Sci.* **2022**, *9*, 2105974, doi:https://doi.org/10.1002/advs.202105974.
40. Li, M.; Wondergem, H.J.; Spijkman, M.-J.; Asadi, K.; Katsouras, I.; Blom, P.W.M.; de Leeuw, D.M. Revisiting the δ-phase of poly(vinylidene fluoride) for solution-processed ferroelectric thin films. *Nat. Mater.* **2013**, *12*, 433-438, doi:10.1038/nmat3577.
41. Li, M.Y.; Wondergem, H.J.; Spijkman, M.J.; Asadi, K.; Katsouras, I.; Blom, P.W.M.; de Leeuw, D.M. Revisiting the delta-phase of poly(vinylidene fluoride) for solution-processed ferroelectric thin films. *Nat. Mater.* **2013**, *12*, 433-438, doi:10.1038/NMAT3577.